

This version of the article has been accepted for publication, after peer review, and is subject to [Springer Nature's AM terms of use](#), but is not the Version of Record and does not reflect post-acceptance improvements, or any corrections. The Version of Record is available online at:

2025, Nature, 643, 645-648 doi:10.1038/s41586-025-09236-z

Close-in planet induces flares on its host star

Ekaterina Ilin^{1,2*}, Harish K. Vedantham^{1,3}, Katja Poppenhäuser^{2,4},
Sanne Bloot^{1,3}, Joseph R. Callingham^{1,5}, Alexis Brandeker⁶,
Hritam Chakraborty⁷

¹*Netherlands Institute for Radio Astronomy, ASTRON, Oude
Hoogeveensedijk 4, Dwingeloo, 7991 PD, The Netherlands.

²Leibniz-Institut für Astrophysik Potsdam, AIP, An der Sternwarte 16,
Potsdam, 14482, Germany.

³Kapteyn Astronomical Institute, University of Groningen, P.O. Box
800, Groningen, 9700 AV, The Netherlands.

⁴Institut für Physik und Astronomie, Universität Potsdam,
Karl-Liebknecht-Str. 24/25, Potsdam-Golm, 14476, Germany.

⁵Anton Pannekoek Institute for Astronomy, University of Amsterdam,
Science Park 904, 1098 XH, Amsterdam, The Netherlands.

⁶Department of Astronomy, Stockholm University, AlbaNova University
Center, Stockholm, 10691, Sweden.

⁷Geneva Observatory, University of Geneva, Chemin Pegasi 51, Versoix,
1290, Switzerland.

*Corresponding author(s). E-mail(s): ilin@astron.nl;

Contributing authors: vedantham@astron.nl; kpoppenhaeger@aip.de;
bloot@astron.nl; callingham@astron.nl; alexis@astro.su.se;
hritam.chakraborty@unige.ch;

Abstract

In the past decade, hundreds of exoplanets have been discovered in extremely short orbits below 10 days. Unlike in the Solar System, planets in these systems orbit their host stars close enough to disturb the stellar magnetic field lines [1]. The interaction can enhance the star's magnetic activity, such as its chromospheric [2] and radio [3] emission, or flaring [4]. So far, the search for magnetic star-planet interactions has remained inconclusive. Here, we report the first detection of planet-induced flares on HIP 67522, a 17 million-year-old G dwarf star with two known close-in planets [5, 6]. Combining space-borne photometry from TESS

and dedicated CHEOPS observations over a span of 5 years, we find that the 15 flares in HIP 67522 cluster near the innermost planet’s transit phase, indicating persistent magnetic star-planet interaction in the system. The stability of interaction implies that the innermost planet is continuously self-inflicting a six time higher flare rate than it would experience without interaction. The subsequent flux of energetic radiation and particles bombarding HIP 67522 b may explain the planet’s remarkably extended atmosphere, recently detected with the James Webb Space Telescope [7]. HIP 67522 is therefore an archetype to understand the impact of magnetic star-planet interaction on the atmospheres of nascent exoplanets.

Keywords: star-planet interaction, stellar flares, HIP 67522, space-borne photometry

HIP 67522 is a young, 17 million year old star-planet system in the Upper Centaurus Lupus part of the Sco-Cen OB association [5, 8] about 125 pc away [9]. The star is a $1.2M_{\odot}$ dwarf [5] that hosts one gas giant planet in a 6.95 d orbit [5], and another in a 14.33 d orbit [6].

The innermost planet orbits less than 12 stellar radii away from the star [5], likely placing it in the sub-Alfvénic regime [1, 10]. In this regime, perturbations of the stellar magnetic field induced by the planet can travel back to the star along the magnetic field lines that tether the two bodies [1] (Fig. 1). The expected power of magnetic star-planet interaction of HIP 67522 with its innermost planet is about 10^{26} erg/s – among the highest powers expected from systems with known close-in companions [11]. In other star-planet systems, magnetic interaction has been suggested to power chromospheric hot spots [2], polarized radio emission [3, 12, 13], and flares [14], but none could be validated in follow-up observations, potentially due to changing magnetic field properties throughout stellar activity cycles [15]. Lacking reliable detections of planet-induced emission so far, the underlying mechanism of energy dissipation remains poorly understood. However, regardless of how the energy is deposited in the star’s atmosphere, the fingerprint of magnetic star-planet interaction is the occurrence of emission that is modulated in phase with the orbit of the interacting planet. This periodic signature is unique as long there is no other comparable periodicity in the system, e.g., the rotation of the star.

HIP 67522 was previously observed by the Transiting Exoplanet Survey Satellite (TESS, [16]) in Sectors 11 (May 2019), 38 (May 2021), and 64 (April 2023) at a 2-min cadence for a total of 65.6 d (Extended Data Fig. 1). Additionally, we gathered dedicated observations of the HIP 67522 system with the CHaracterising ExoPlanets Telescope (CHEOPS, [17]) for a total of 7.6 d between March 9 and June 22, 2024 (Extended Data Table 1). We achieved excellent phase coverage: each hour of the 167 h orbit of HIP 67522 b was fully covered at least seven times (Fig. 3 and Extended Data Table 2). We detected 12 flares in the TESS light curves (Extended Data Fig. 2), and 4 in the CHEOPS light curves (Extended Data Fig. 3, see also Methods). Of the CHEOPS flares, 3 were above the detection threshold for TESS. We use these for analysis, giving a total of 15 flares (Extended Data Table 3), to ensure that the different detection thresholds for flares in CHEOPS and TESS do not bias our conclusion.

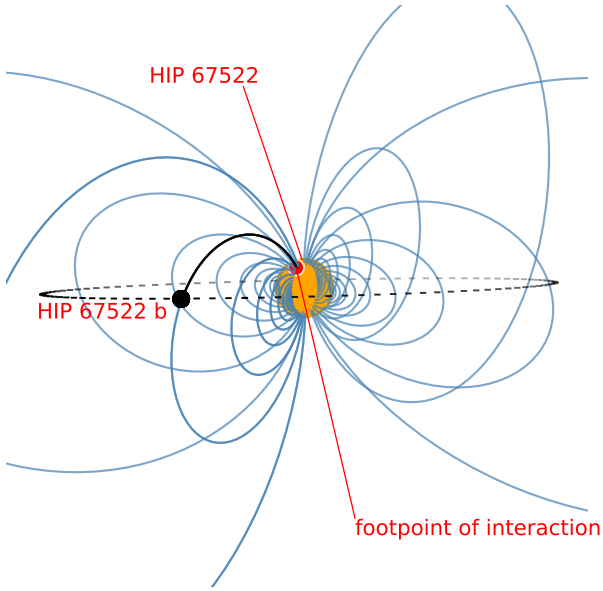


Fig. 1: Magnetic star-planet interaction in the HIP 67522 system. HIP 67522 b is shown as it perturbs the star’s inclined magnetic field. The perturbation travels along the magnetic field line highlighted in black, toward the stellar surface, where it triggers flares at the footpoint.

Fig. 2 shows the flare rate computed from the 15 flares as a function of the orbital phase of HIP 67522 b. The flare rate is highly elevated shortly after transit: we detect 11 flares in the orbital phase range 0–0.2 and only 4 flares throughout the rest of the orbit, amounting to an almost nine times higher flare rate in the 0–0.2 phase range. We confirmed the statistical significance of this elevated flare rate with a simple calculation. The 4 flares yield a base flare rate of 0.07 flares per day, accounting for the observing time spent on the 0–0.2 range. Based on this flare rate, we anticipate an average of only 1.3 flares in the 20% range. Detecting 11 flares or more by chance at this base rate can be excluded with high confidence ($p < 0.001$ [18]). Similarly, a Rayleigh test for uniformity on circular data applied to the TESS observations only, which sample the orbital phase roughly uniformly, indicates a clustering with a p-value of 0.0145. To include the CHEOPS observations, and ensure that our analysis is not biased by an a posteriori choice for the preferred 0–0.2 phase range, we implemented a Bayesian model selection that accepts the preferred range of elevated flaring as a free parameter. In this analysis, we calculate the total observing time per orbital phase bin, ensuring that the bin size is smaller than the clustering range, covering no more than 2% of the orbit in each bin. We then compare two models that may explain the number of flares detected in each of these bins. The first model represents intrinsic stellar flaring without star-planet interaction. In this model, flares have no dependence

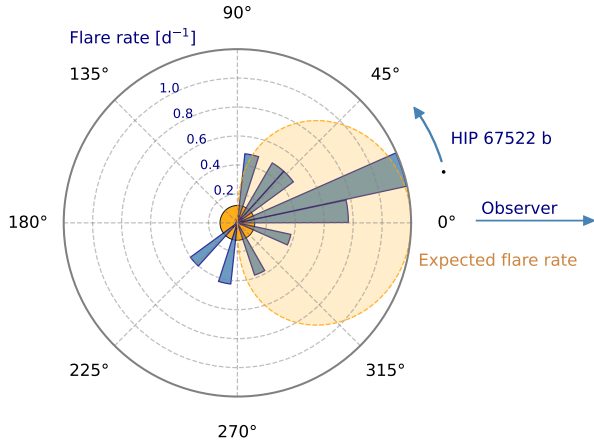


Fig. 2: Observed flare rates on HIP 67522 along the orbit of its innermost planet, HIP 67522 b. A significant flare rate increase in the expected range suggests most detected flares were planet-induced. The orange dashed region marks the expected flare rate from an interaction footpoint at the sub-planetary longitude. These flares are visible only when the planet faces the observer ($[-90^\circ, +90^\circ]$) and are most likely near transit (0°).

on orbital phase, such that the Poisson occurrence rate of flares in each time bin is the same. The second model allows a section of the orbit to show a different flare rate at the cost of three additional parameters in the second model, i.e., the second flare rate, the starting phase, and the width of the section with modulated flaring. Despite the added complexity, we find that the second model is strongly preferred over the first, with the ratio of the two marginal likelihoods, i.e., the Bayes Factor, of 11.7, and a difference in the Akaike Information Criterion between the models of 7.5. These results are robust against variation in the bin sizes down to 0.5% of the orbit (Methods, Extended Data Figure 4).

Our Bayesian analysis shows that the base flare rate outside the clustered region is $0.09^{+0.06}_{-0.04} \text{ d}^{-1}$ above 10^{34} erg , and that it is elevated to $0.59^{+0.38}_{-0.22} \text{ d}^{-1}$, i.e., by a factor of 6, for $20^{+11}_{-12}\%$ of the orbit of HIP 67522 b, beginning around transit (Fig. 3). This orbital range is consistent with the clustering range that is expected considering the geometry of the system (orange shadow in Fig. 2): The planet orbits at low eccentricity [5, 6], and the stellar rotational and planetary orbital axes are aligned [19] (Methods). The visibility of flares at the footpoint of interaction for the observer is modulated by the optical self-shadowing of flares. Planet-induced flares can be best detected when the footpoint is closest to the center of the stellar disk, worst near the limb, and not at all when it is behind the stellar disk as seen from the Earth. The limited observing time and sensitivity further restrict the detected clustering to phases near transit. If the large-scale magnetic field is well-described by a dipole field aligned with the rotation axis nearly in the plane of the sky [5, 19], the clustering would center

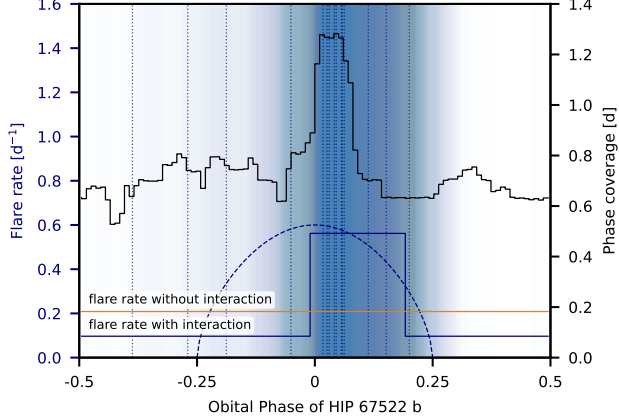


Fig. 3: Best-fit flaring models. Models are either with (dark blue) or without (orange) planet-induced flaring. The blue shading indicates expected elevated flare rates based on observed flares (dotted lines) and phase coverage (black line), with darker shade marking higher probability. The relative expected flare rate at the sub-planetary point (orange arc) is consistent with the measured phase range of elevated flaring.

on transit, and the least flares would be observed when the planet is behind the star from the point of view of an observer on the Earth. As any cool dwarf, HIP 67522 also produces energetic flares intrinsically, so the flare rate need not be zero when the footprint of interaction is not in view.

In the simplest physical scenario, we can assume that the planet orbits within a misaligned stellar dipole magnetic field (Fig. 1). Higher order multipole modes fall off faster with distance than the dipole mode, so that it likely dominates at the location of HIP 67522 b (see Methods). Due to the star’s fast rotation, the planet encounters periodic maxima and minima in magnetic field strength multiple times per orbit. The varying field induces an additional modulation in the star-planet interaction strength (Fig. 4), which depends on the position of the footprint, and the stellar magnetic field strength at the planet’s location [1, 20]. Over time, the additional modulation averages out, and reduces the observed modulation to a modulation similar to the optical self-shadowing. In Fig. 4, the averaged model marginalizes over the full range of dipole axis orientations, showing that it is robust against a possible unstable dipole axis [21, 22]. The additional modulation is only preserved when the rotational and orbital period are exact multiples of each other. In that case, the center of the main cluster may be offset from mid-transit. In our data, the flare cluster is at phase 0.08 ± 0.04 , consistent with being centered on transit within 2σ , so a resonance is not required to explain the data. Yet, with a rotation period of approximately 1.418 ± 0.016 d [5], HIP 67522 b orbits near a 1:5 commensurability between the rotation period of the star and the orbital period of HIP 67522 b. If this resonance was

exact, the planet could align with the same stellar longitude at fixed orbital phase, and produce a peak of clustering offset from mid-transit (Fig. 4).

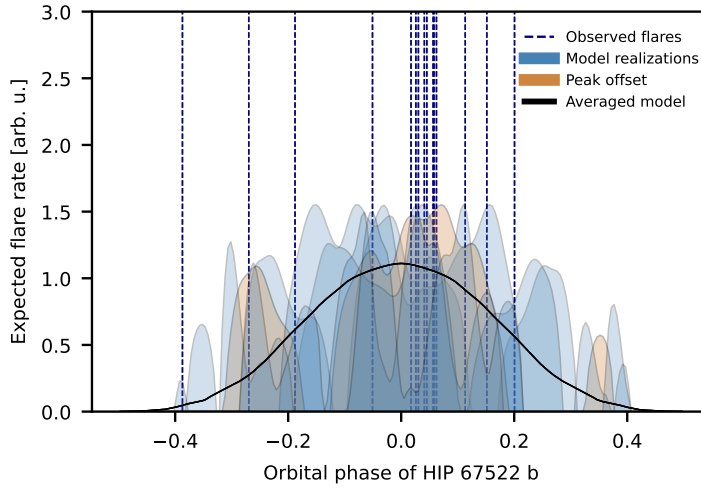


Fig. 4: Flaring interaction with an oblique, dipolar stellar magnetic field. Flare rates (blue filled curves), averaged over time and obliquity, become dominated by geometric foreshortening (black line). Under exact 1:5 spin-orbit commensurability, the modulation at the synodic period of the planet can be preserved, and produce a peak marginally offset from transit (orange filled curve), as observed for HIP 67522.

The detection of magnetic star-planet interaction in HIP 67522 is not a coincidental effect of testing a large sample of candidates. Among the few dozen flaring star-planet systems known to date, less than ten host a planet potentially close enough to be within the sub-Alfvénic zone of the star’s magnetosphere, and induce flares on its host star [10]. Among those few, HIP 67522 has one of the highest predicted powers of magnetic interaction [10].

The energy distribution of planet-induced flares follows a power law with index ~ -1.6 . The distribution can be integrated to obtain the total power emitted in the interaction, which is determined by the high energy cutoff. Setting this cutoff conservatively to the energy of the largest observed flare, we obtain a power of $4.6 \cdot 10^{29}$ erg/s (Extended Data Fig. 5). This is likely an underestimate, possibly up to a factor of 5, because the optical TESS and CHEOPS bandpasses miss both the contribution of the X-ray and near-UV components [23–25]. Both are important for planetary photochemistry and atmospheric heating.

The available energy flux in the Alfvén wing framework [1] depends on the planetary magnetic field strength B_p and stellar wind parameters. While the latter can be measured in some cases [26], no planetary magnetic fields have been reliably detected to date. Regardless, we find that the measured planet-induced flux cannot be supplied in the Alfvén wing framework even with liberal assumptions on B_p and stellar wind

parameters (Methods). We therefore suggest that the power in planet-induced flares in HIP 67522 is supplied by the energy reservoir stored in the star’s coronal loops. The interaction may propagate along a potential large-scale field toward the footpoint in the corona, where it then triggers flares in the small-scale non-potential coronal field (a similar mechanism was suggested by [27]). Such a mechanism would have to tap about 15% percent of the $3 \cdot 10^{30}$ erg/s coronal X-ray luminosity of HIP 67522 [28] in order to match the measurement. We note, however, that the X-ray luminosity was derived from observations conducted shortly before the transit of HIP 67522 b, and may therefore represent a level of emission already elevated by (flaring) interaction.

Regardless of the underlying mechanism, the observed planet-induced emission has striking consequences. The orbital phases of the flares induced by HIP 67522 b imply that the interaction with the star backfires on the planet through self-inflicted space weather. A planet’s space weather denotes the bombardment with high energy radiation and particles that erodes its atmosphere, and determines its ultimate mass and radius over cosmic time scales. Based on our results, HIP 67522 b is continually exposed to a roughly six times higher flare rate than it would be without interaction. Observations with the James Webb Space Telescope suggest that the bulk density of HIP 67522 b is extremely low: Despite its Jupiter-sized radius, its mass was constrained to less than $0.05M_{\text{Jup}}$, with a best-fit mass of $15M_{\oplus}$ [7]. The low mass and strong irradiation by its young host star are considered the main reasons for the high inflation of HIP 67522 b’s atmosphere [7, 28]. The total amount of mass lost in the upcoming 100 million years will determine whether HIP 67522 b becomes a hot Neptune type planet, or will further erode and lose a significant fraction of its atmosphere to become a smaller, sub-Neptune object [7]. Our results suggest that previous estimates, although already indicating considerable mass loss [7, 28] from high energy radiation, may still be underestimating the total mass loss rate that can occur in HIP 67522 b under the exposure to the elevated flare rate at the sub-planetary longitude and associated planet-ward coronal mass ejections (CME). On the Sun, large flares are typically associated with CMEs. On other stars, a CME is estimated to carry roughly the same the energy as the flare itself [29]. If a CME is launched from the footpoint of flaring interaction near the sub-planetary point, it is much more likely to hit the planet than if the CME was triggered in random locations on the star. Numerical models suggest significant stripping of exoplanet atmospheres under the impact of CMEs [30, 31], particularly when the atmosphere is already expanded due to radiative heating [32, 33]. Under energy-limited escape, assuming an efficiency of 10% and CME angular widths typically observed on the Sun ($50^\circ - 80^\circ$ [34]), the impact of planet-induced CMEs would increase the mass loss rate derived from quiescent X-ray und UV flux [7] by 50 – 130% (Extended Data Fig. 6). Consequently, self-induced flaring may considerably shorten the lifetime of the planet’s atmosphere from 1000 to about 400 – 700 million years.

Our results establish HIP 67522 as the archetype system for flaring star-planet interaction. HIP 67522 is the first star-planet system where the interaction persisted over a minimum of three years. This reliability opens the door to follow-up observations, and urges the characterization of HIP 67522 c to allow for differential analysis of the two planets in the system. The well-known properties of HIP 67522 and

HIP 67522 b allow us to target similar systems with a high probability of such interaction, such as V1298 Tau and TOI-837. With deeper understanding of the sub-Alfvénic environment of planets like HIP 67522 b, magnetic star-planet interaction will not only probe exoplanetary space weather, but will also be instrumental for constraining their elusive magnetic fields [1, 20] Planetary space weather and magnetic fields are crucial for understanding their atmospheric dynamics, assessing habitability, and probing interior compositions – key to unraveling how planets throughout the Milky Way, including those in our Solar System, have formed and evolved.

Methods

Photometric Data Reduction

For the TESS photometry, we used the PDC_SAP 2-min cadence light curves reduced by the Science Processing Operations Center (SPOC), available from the Mikulski Archive for Space Telescopes (MAST). For the CHEOPS photometry, we obtained 10 s imagette exposures (AO-4 ID4, PI: E. Ilin; AO-4 ID17, PI: H. Chakraborty), and used the open source photometric extraction package PIPE¹ v1.1, designed to enable point-spread function (PSF) photometric extraction from the CHEOPS imagettes [35]. PSF photometry also reduces the roll modulation of CHEOPS data caused by the field of view rotating once per orbit in combination with background stars and an asymmetric PSF. We derived custom PSF models using data from the observations themselves, as described by the PIPE manual². We removed flagged data points from all TESS and CHEOPS light curves prior to searching them for flares.

Flare Detection

Flare detection follows three steps: removal of astrophysical variability, automatic identification of flare candidates, and confirmation of bona fide flares through visual inspection and ancillary data.

We removed the variability from the TESS light curves using the approach detailed in [10]. The CHEOPS data could not be treated in the same way because of the much shorter observing baselines and frequent gaps in the observations. We modeled each 13 – 23 h CHEOPS visit individually with a combination of the `batman` [36] transit model for HIP 67522 b with quadratic limb darkening using the planetary orbital and limb darkening parameters from [6], and a 5th degree polynomial to approximate the star’s rotational variability. Three large flares and all data points with a CHEOPS quality flag > 0 were masked prior to fitting the model using a least-square fit (`scipy.curve_fit`, [37]). We then subtracted the model from the data, and masked all outliers above 4 standard deviations in the residuals. We repeated the model fit with the updated mask to obtain the final model. The model was then subtracted again from the data, and we applied a Savitzky-Golay [38] filter to smooth the remaining non-flaring variability. For the filter, we chose a 3rd order polynomial, and a window that was 20% of the total length of each visit with CHEOPS. As a final correction, we

¹<https://github.com/alphapsa/PIPE>

²https://github.com/alphapsa/PIPE/blob/4d592ac796e57a7accfb78bbea96577b90eceb71/docs/pipe/PIPE_manual.pdf

subtracted the remaining roll dependent systematics that were not captured by PIPE using the median of the 100 closest data points in roll angle as the truth for any data point in the light curve.

For the initial flare identification from the resulting flattened light curves, we followed the approach in [10], where three consecutive data points three standard deviations above the noise level define a candidate event. The noise levels of the CHEOPS and TESS light curves are similar, 810 ± 90 ppm and 780 ± 70 ppm at 10 s and 120 s cadence, respectively, defined as the standard deviation of the de-trended light curves. Despite the similar noise levels, the energy detection threshold for CHEOPS is more than an order of magnitude lower than that of TESS because of its bluer passband and higher time resolution, which make CHEOPS more sensitive to flares. Consequently, for the statistical analysis, the CHEOPS flare with a lower energy than TESS was excluded from the statistical analysis.

The resulting candidates were manually inspected, for a total of four bona fide flares in the CHEOPS light curves, and twelve in the TESS light curves. We rejected several false positive candidates in CHEOPS, because their occurrence was invariably connected to a steep rise in background flux, or repeated roll angle modulation. In TESS, we found no false positives. We validated that the 16 final flares were indeed associated with the star by verifying the absence of moving objects in the field or variability associated with the entire image in the pixel level data.

Flare Energy

We characterized each flare by fitting an empirical, analytic, continuous flare template [39] to its light curve. The baseline flux was established using the same technique used to de-trend the CHEOPS light curves. We first estimated the best parameters with a least-square fit (`scipy.curve_fit`, [37]), then used the results to efficiently sample the posterior distribution with the Markov-Chain Monte Carlo method (`emcee`, [40]), assuming flat priors for all flare parameters, i.e. the flare amplitude, full width at half maximum, and peak time of the flare.

We calculated the bolometric energy of the flares following the prescription in [41], which converts the flux emitted by the star and the flare in the TESS and CHEOPS passbands to the bolometric emission from the flare. We assumed the temperatures of both the star and the flare as known. We propagated the posterior distribution of the flare parameters to derive the bolometric flare energy using Gaussian distributions for the stellar radius $R_* = 1.39 \pm 0.06$ [5] and effective temperature $T_{\text{eff}} = 5650 \pm 75$ [5]. We assumed that the flares were black body emitters with a temperature of 10^4 K. We note that, on the one hand, the flare temperature can vary greatly [42, 43]. On the other hand, the flare energy is not very sensitive to the assumed flare temperature when using the prescription in [41].

Characterizing the Clustering of Flares in Orbital Phase

To ascertain that the clustering of flares was a true clustering event, and not a confluence of random occurrences of intrinsic flares, we cast the two possible scenarios as Bayesian models, one with and one without flare clustering. The first model M_{unmod}

assumes the absence of any modulation, i.e., that no clustering is present, so that the data can be reproduced by a single Poisson flare rate λ_0 . The expected number of flares x_i per phase bin i is then determined by the total observing time t_i in that phase bin:

$$x_i = \lambda_0 t_i \quad (1)$$

The individual observed numbers of flares n_i are independent of each other, so that the likelihood of a single flare rate λ_0 representing the full set of observations D split into k bins as $D = [n_1, \dots, n_k]$ reads:

$$P(D|\lambda_0) = \prod_{i=1}^k \frac{e^{-\lambda_0 t_i} (\lambda_0 t_i)^{n_i}}{n_i!} \quad (2)$$

We have no prior information about λ_0 , which we can represent as Jeffrey's prior:

$$P(\lambda_0) = \frac{1}{2\sqrt{2\lambda_0}} \quad (3)$$

Jeffrey's prior is improper, i.e., the integral over all $\lambda_0 \geq 0$ is not finite, so we limit $0 < \lambda_0 < 2 \text{ d}^{-1}$, where the upper limit is above the highest flare rate found for stars with similar spectral type and fast rotation across the TESS sky in [44] above the minimum detected flare energy in our flare catalog (Extended Data Figure 7). This upper limit is conservative, and likely an overestimate because the sample in [44] also includes extremely active BY Dra type variables. The $\sqrt{2}$ in the denominator is the normalization factor $N = \int_0^2 \lambda_0^{-1/2} d\lambda_0$. Following Bayes' theorem, the probability of λ_0 given the data is

$$P(\lambda_0|D) = \frac{P(D|\lambda_0)P(\lambda_0)}{P(D)}, \quad (4)$$

with the marginal likelihood

$$P(D) = P(M_{\text{unmod}}) = \int_0^2 d\lambda_0 P(D|\lambda_0)P(\lambda_0). \quad (5)$$

The second model, M_{mod} , assumes that the presence of a modulation, such that there is an orbital phase range $(\phi_0, \phi_0 + \Delta\phi)$ during which the flare rate is $\lambda_1 \neq \lambda_0$, such that

$$x_i = \begin{cases} \lambda_1 t_i & \phi_0 < \phi_i < \phi_0 + \Delta\phi, \text{ and} \\ \lambda_0 t_i & \text{else.} \end{cases} \quad (6)$$

We note that the phase bins i must be small compared to the extents of the two phase ranges in order for each bin to be uniquely attributed to either range. The corresponding likelihood for the full set of parameters, $\Theta = [\lambda_0, \lambda_1, \phi_0, \Delta\phi]$,

$$P(D|\Theta) = \prod_i^k \begin{cases} \frac{e^{-\lambda_1 t_i} (\lambda_1 t_i)^{n_i}}{n_i!} & \phi_0 < \phi_i < \phi_0 + \Delta\phi \\ \frac{e^{-\lambda_0 t_i} (\lambda_0 t_i)^{n_i}}{n_i!} & \text{else} \end{cases}, \quad (7)$$

and uninformative prior,

$$P(\Theta) = 2 \frac{1}{2\sqrt{2\lambda_0}} \frac{1}{2\sqrt{2\lambda_1}}, \quad (8)$$

assume that λ_0 and λ_1 are independent, and take values between 0 and 2. We did not make assumptions about where the clustering begins (ϕ_0) or how wide the clustering phase range is ($\Delta\phi$). Therefore, we let ϕ_0 run from 0 to 1 with equal probability. We restrict $\Delta\phi$ from 0 to 0.5 so that we avoid double-counting the identical solution pairs generated by the substitutions: $\phi_0 \rightarrow \phi_0 + \Delta\phi$, $\Delta\phi \rightarrow 1 - \Delta\phi$, $\lambda_0 \rightarrow \lambda_1$ and $\lambda_1 \rightarrow \lambda_0$ (Note that we do not impose $\lambda_1 > \lambda_0$). Normalization of the prior probability of $\Delta\phi$ contributes the factor of 2 to the prior. The marginal likelihood for M_{mod} is:

$$\begin{aligned} P(D) &= P(M_{\text{mod}}) \\ &= \int_0^2 d\lambda_0 \int_0^2 d\lambda_1 \int_0^1 d\phi_0 \int_0^1 d\Delta\phi P(D|\Theta)P(\Theta) \end{aligned} \quad (9)$$

We sampled the posterior distribution with `emcee` [40] to obtain uncertainties on the best-fit parameters for the model (see following Section). To decide which model better represents the data, we calculated the Bayes factor, that is the ratio of the two marginal likelihoods,

$$K = \frac{P(M_{\text{mod}})}{P(M_{\text{unmod}})}. \quad (10)$$

The Bayes factor penalizes the increase in the number of parameters in M_{mod} , as the integral must be performed over a much larger parameter space in Eq. 9 compared to Eq. 5. The two equations can be solved numerically. We chose a sufficiently high grid size of 400, 400, 100, and 50 for λ_0 , λ_1 , ϕ_0 and $\Delta\phi$. We further chose bin widths between 0.5% and 2% of the orbit, such that possible small widths of the clustering phase range $\Delta\phi$ could be sufficiently well sampled, and no phase information was lost due to coarse binning. The resulting Bayes factors varied from bin size to bin size, with a mean and standard deviation of 11.7 ± 1.9 . The average Bayes factor increases slightly toward smaller bin sizes, but the trend flattens out above 75 bins at $K = 11.8 \pm 1.6$.

Besides the Bayes factor, we also computed the Akaike Information Criterion (AIC) from the best-fit results obtained from sampling the posterior with `emcee`, where each best-fit parameters are defined as the 50th percentile of the posterior distribution. The AIC is an approximation to the Bayes factor that compares the likelihoods of the best-fit solutions instead, while penalizing the number of parameters in the model. We tested bin widths between 0.5% and 2% of the orbit, for an average and standard deviation in the difference of AIC values between the two models of 7.5 ± 1.4 in favor of the modulated model, and 7.5 ± 1.3 above 75 bins.

Energetics

In the unmodulated flaring model, the best-fit flare rate is $\lambda_0 = 0.21^{+0.06}_{-0.05} \text{ d}^{-1}$ above the minimum detected flare energy of $1.0 \times 10^{34} \text{ erg}$, consistent with the simple division of 15 flares by the total observing time of 73.2 d. For the modulated flaring model, the

flare rate outside the clustering range is lower, $\lambda_0 = 0.09^{+0.06}_{-0.04} \text{ d}^{-1}$. The planet-induced flaring rate is roughly six times higher than the base rate, at $\lambda_1 = 0.60^{+0.38}_{-0.22} \text{ d}^{-1}$. The flare rate is elevated starting at around transit, i.e., $\phi_0 = 0.00^{+0.02}_{-0.08}$, and lasts for about 20% of the orbit, i.e., $\Delta\phi = 0.20^{+0.11}_{-0.12}$. The best-fit values and uncertainties are defined by the 16th, 50th and 84th percentiles of the posterior distribution for each parameter. Uncertainties are similar for different bin sizes ≥ 75 , and median values vary an order of magnitude less across bin sizes than for any individual bin size. For the most accurate best-fit value, we quote the mean across all 50th percentiles for bin sizes 75 – 200.

We calculated the flux emitted in flares through planet-induced flaring by extrapolating the flare frequency distribution to lower and higher flare energies. We used the difference in flare rate $\lambda_1 - \lambda_0$ and the power law slope $\alpha \approx 1.6$ derived from the flare frequency distribution of the full sample of 15 flares following the method in [45]. There is no significant difference in energy distribution between the planet-induced and intrinsic flare sub-samples. Since the power law slope is $\alpha < 2$, the total flux is dominated by high energy flares. For a conservative estimate, we set the maximum energy of planet-induced flares to the highest flare energy detected in the elevated flaring range, that is $7.4 \times 10^{35} \text{ erg}$. Flares at and above this energy occur on a monthly basis. With the chosen maximum energy, the total flux in planet-induced flares is $4.6 \times 10^{29} \text{ erg/s}$. Even if the three highest energy events out of the 11 flares in the elevated flaring region were not planet-induced but stemmed from the intrinsic λ_0 contribution, the planet-induced flux would still be $> 10^{29} \text{ erg/s}$.

The planet-induced flare flux is considerably higher than the interaction flux expected in the Alfvén wing model [1], even under very generous assumptions. Using the same procedure as in [10], we calculate the average magnetic field strength of HIP 67522 from its X-ray luminosity from [28], and alternatively, from its Rossby number, following [46], which yield 3.1 and 2.1 kG, respectively. For planetary magnetic fields $B_p = 0.01 - 100 \text{ G}$, stellar wind densities at the coronal base of $\rho = 0.1 - 100\rho_\odot$ ($\rho_\odot = 10^{10} \text{ cm}^{-3}$), and stellar average magnetic field strengths $B = 1600 - 3500 \text{ G}$, the star-planet interaction flux yields $10^{24} - 10^{28} \text{ erg/s}$, where the strongest flux is obtained with the highest values in the given ranges. Therefore, it is unlikely that the Alfvén wing interaction alone powers the elevated flaring in HIP 67522.

Geometric Model of Flaring Star-Planet Interaction

A clustering of flares in HIP 67522 within the observed phase range can be explained under minimal assumptions about the system's architecture and magnetic field. In the general case, we consider a dipole magnetic field inclined by an angle α relative to the rotational axis i , which we assume to be edge-on ($i = 90^\circ$), with the planetary orbit lying in the same plane, consistent with observational constraints [19]. We assume a purely dipolar large-scale stellar magnetic field, which is not generally true, as, e.g., the Sun is dominated by higher order multipole during certain phase of its cycle [47]. However, a dipolar component, as inferred within the capabilities of Zeeman Doppler Imaging [48] in Sun-like stars, is usually significant [49, 50], and is likely to dominate at far out distances from the stellar surface. As the planet moves through the

stellar magnetosphere, the field lines connecting the star and planet trace back to specific footpoints on the stellar surface. The visibility of these flaring footpoints in the observer's frame depend on their position on the star, and the self-shadowing effects of the optically thick flare emission regions as they rotate across the stellar disk. Among the two footpoints associated with a given interaction, the one with the shortest path along the field line dominates, which is always on the hemisphere facing the planet. The measurable flux F_{SPI} from the dominant footpoint is proportional to the local magnetic field strength $\propto B^\beta$ (with $\beta > 0$; [1, 20]) at the planet's position, and is modulated by the self-shadowing term $\cos \theta \cos \phi$, where θ and ϕ are the latitude and longitude of the interaction footpoint. To relate this to the observed flare rate, F_{SPI} is taken to the exponent $\alpha - 1 \approx 0.6$. Additionally, we assume that HIP 67522 b remains within the sub-Alfvénic zone throughout its orbit, so that interaction can take place anytime.

A model realization in Fig. 4 is defined as the flare rate for a given obliquity of the dipole axis, and longitude relative to the planet's orbital phase for one orbit of the planet. The visibility of planet-induced flares is mainly determined by the self-shadowing of optical flares, leading to the bell-shaped distribution of expected flare rates shown in Fig. 4. However, if the system exhibits a specific spin-orbit commensurability, such as the proposed 1:5 resonance between the stellar rotation and planetary orbit, the interaction pattern becomes more complex, with additional peaks modulated by the synodic period of HIP 67522 b. This additional periodicity can shift the apparent clustering of flares away from the planetary transit phase, and possibly explain the observed phase offset in planet-induced flare activity.

Further Discussion

Further discussion of flare properties, the relation between rotational and orbital modulation of flares, and the posterior probability distributions of the model parameters can be found in the transparent peer review documents associated with this manuscript, among others topics.

Declarations

Acknowledgements: We would like to thank Julián Alvarado-Gómez for helpful discussions regarding CME-driven mass loss.

Funding: E.I. and H.K.V. acknowledge funding from the European Research Council under the European Union's Horizon Europe programme (grant number 101042416 STORMCHASER). K.P. acknowledges funding from the German *Leibniz-Gemeinschaft* under project number P67/2018. S.B. acknowledges funding from the Dutch research council (NWO) under the talent programme (Vidi grant VI.Vidi.203.093). A.Br. was supported by the SNSA. H.C. acknowledge the support of the Swiss National Science Foundation under grant number PCEFP2_194576

Conflict of interest/Competing interests: The authors declare no competing interests or conflict of interest.

Data availability: This paper includes data collected by the TESS mission, which are publicly available from the Mikulski Archive for Space Telescopes (MAST) under

ObsID TIC 166527623. Funding for the TESS mission is provided by the NASA's Science Mission Directorate. CHEOPS data analyzed in this article will be made available in the CHEOPS mission archive (https://cheops.unige.ch/archive_browser/). CHEOPS is an ESA mission in partnership with Switzerland with important contributions to the payload and the ground segment from Austria, Belgium, France, Germany, Hungary, Italy, Portugal, Spain, Sweden, and the United Kingdom. The CHEOPS Consortium would like to gratefully acknowledge the support received by all the agencies, offices, universities, and industries involved. Their flexibility and willingness to explore new approaches were essential to the success of this mission.

Code availability: All code necessary to reproduce the results in this manuscript is available on GitHub <https://github.com/ekaterinailin/hip67522-spi/tree/flaring-spi>.

Author contributions: E.I. and K.P. initiated the star-planet interaction search project. E.I. led the processing of TESS and CHEOPS data with input from A.B., led the energetics and geometric calculations with input from H.K.V. and K.P.. E.I and H.K.V. performed the clustering analysis with input from J.R.C. and S.B.. S.B. provided input on the stellar wind estimate. H.C. aided with the data collection and sharing across projects. All authors commented on the manuscript. Correspondence and requests or materials should be addressed to E.I. (ilin@astron.nl).

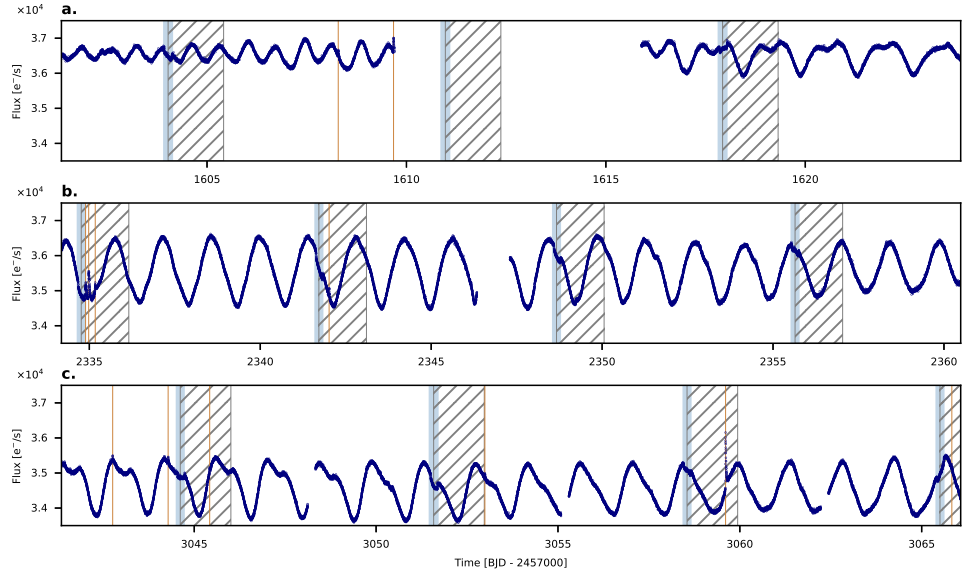
Reprints and permission information is available at www.nature.com/reprints.

Extended Data

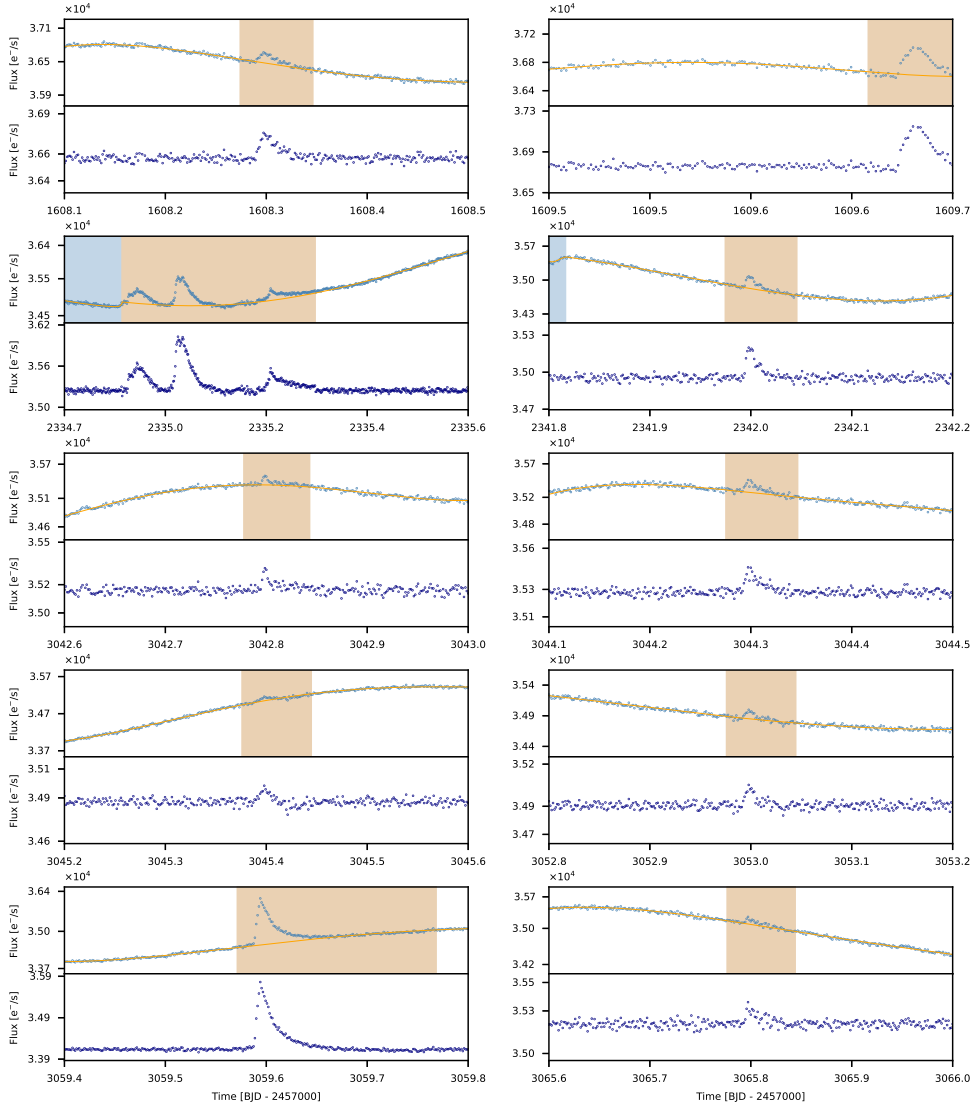
Extended Data Table 1: CHEOPS observing log.

OBSID	File Key	Start Date [UTC]	Obs. baseline [h]
2365179	CH_PR240004_TG000101_V0300	2024-03-09 05:09	13.18
2367052	CH_PR240004_TG000102_V0300	2024-03-16 05:56	13.18
2370611	CH_PR240004_TG000103_V0300	2024-03-23 03:34	13.18
2377976	CH_PR240004_TG000104_V0300	2024-03-30 02:46	13.18
2406487	CH_PR240004_TG000105_V0300	2024-05-10 20:52	13.8
2413239	CH_PR240004_TG000106_V0300	2024-05-17 19:31	13.19
2421684	CH_PR240004_TG000107_V0300	2024-05-24 17:53	15.04
2432394	CH_PR240004_TG000108_V0300	2024-05-31 18:07	13.18
2444115	CH_PR240004_TG000109_V0300	2024-06-07 16:58	13.18
2446774	CH_PR240004_TG000110_V0300	2024-06-14 17:24	14.17
2455494	CH_PR240004_TG000111_V0300	2024-06-21 14:03	13.18
2382459	CH_PR240017_TG000101_V0300	2024-04-05 15:37	19.98
2382460	CH_PR240017_TG000102_V0300	2024-04-12 14:38	19.1
2390044	CH_PR240017_TG000103_V0300	2024-04-19 13:41	22.77
2402938	CH_PR240017_TG000104_V0300	2024-05-03 12:11	19.29
2394579	CH_PR240017_TG000501_V0300	2024-04-28 17:25	15.53
2383621	CH_PR240017_TG000601_V0300	2024-04-11 10:48	15.53
2402943	CH_PR240017_TG000701_V0300	2024-04-30 12:18	15.53
2366465	CH_PR240017_TG000801_V0300	2024-03-11 08:35	17.82
2372811	CH_PR240017_TG000901_V0300	2024-03-21 03:03	16.7
2435119	CH_PR240017_TG001001_V0300	2024-05-26 15:30	16.65
			$\Sigma_{\text{baseline}} = 327.4$
			$\Sigma_{\text{observed}} = 183.0^*$

*Baseline minus the observing gaps caused by the orbit of the spacecraft.



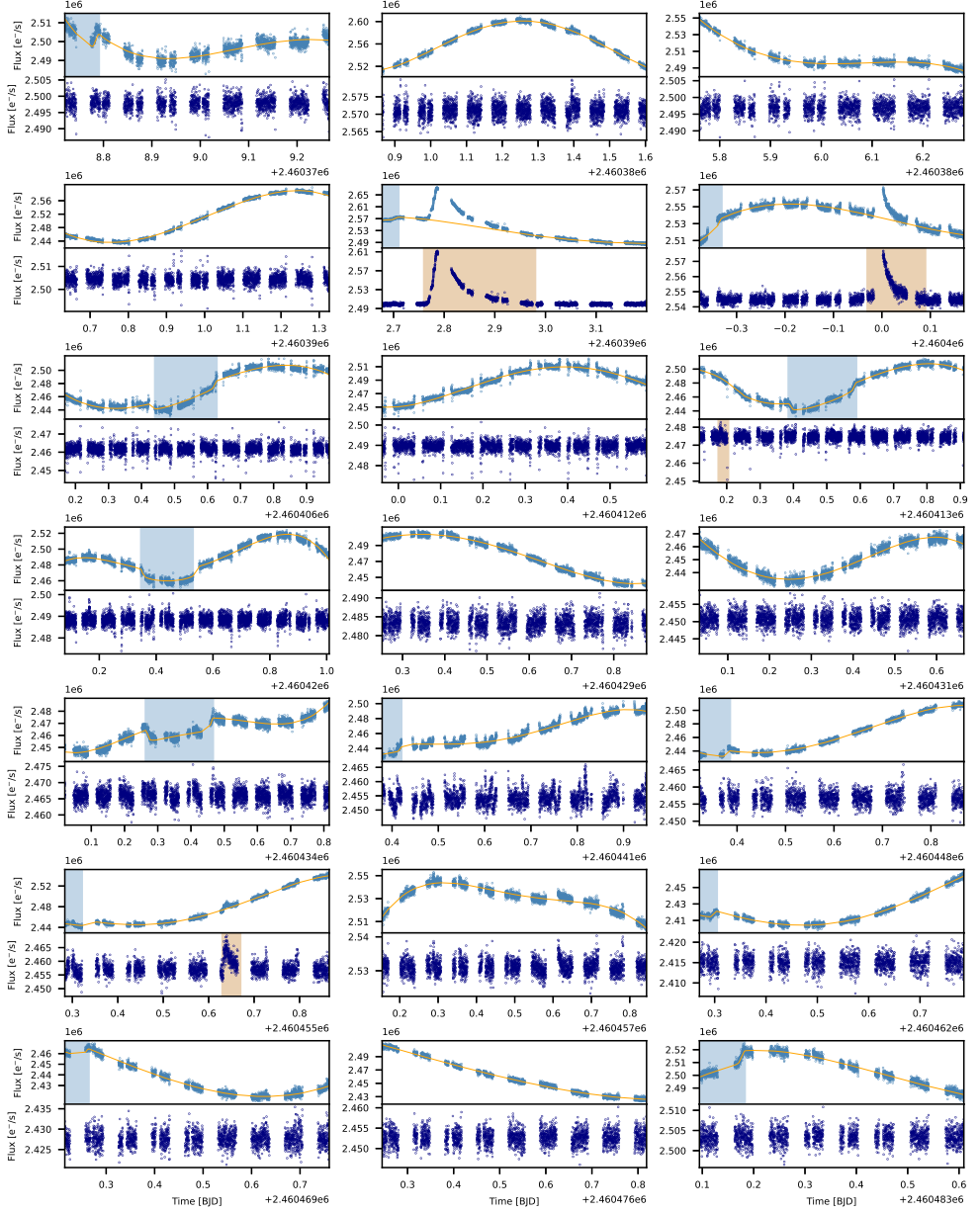
Extended Data Figure 1: TESS light curves of HIP 67522. Blue scatter shows the 2-min TESS PDC_SAP flux. Light blue shades show the batman [36] transit models of HIP 67522 b. Orange vertical lines mark the detected flares, and grey hatched area mark the best-fit window of elevated flare rate.



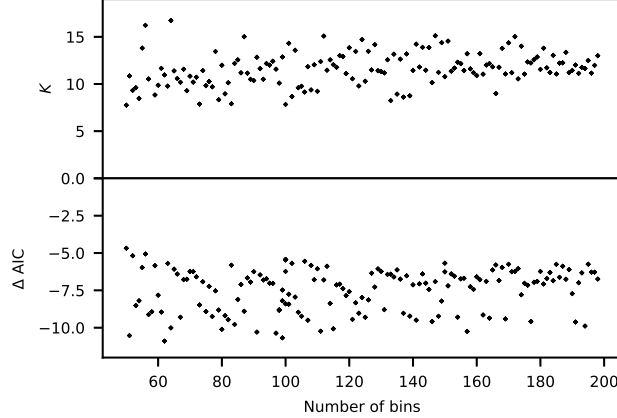
Extended Data Figure 2: Flares in TESS light curves of HIP 67522. Yellow lines show the polynomial fit including the `batman` [36] transit model of HIP 67522 b, highlighted with a blue shade. Each bottom panel shows the residual light curve with the polynomial model and transit removed. The flare template was fit within the orange highlighted region.

References

- [1] Saur, J., Grambusch, T., Duling, S., Neubauer, F. M. & Simon, S. Magnetic energy fluxes in sub-Alfvénic planet star and moon planet interactions. *Astronomy*



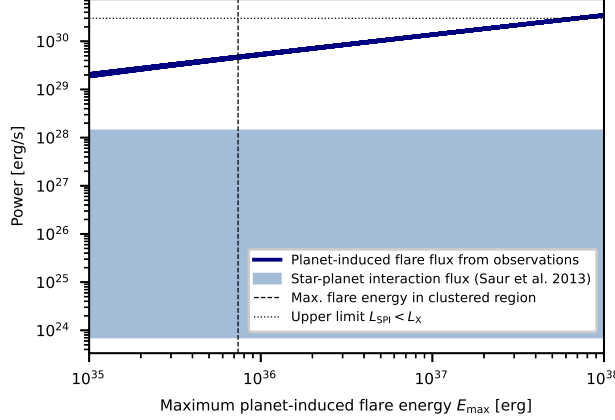
Extended Data Figure 3: CHEOPS light curves of HIP 67522. Top panels show the PIPE reduced 10-s cadence imagette light curves as blue scatter. Yellow lines show the polynomial fit including the `batman` [36] transit model of HIP 67522 b, highlighted with a blue shade. Each bottom panel highlights flares within the orange shaded regions, which are reintroduced into the residual light curve (blue scatter).



Extended Data Figure 4: Bayes Factor and Akaike Information Criterion.
The values for both statistics converge above 75 orbital phase bins, indicating that the phases are sufficiently resolved.

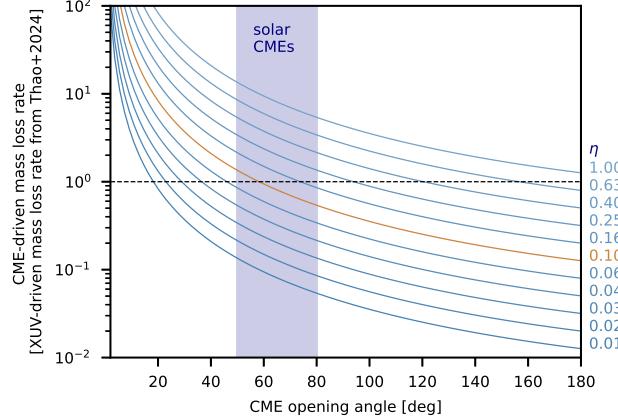
and Astrophysics **552**, A119 (2013).

- [2] Shkolnik, E., Walker, G. A. H. & Bohlender, D. A. Evidence for Planet-induced Chromospheric Activity on HD 179949. *The Astrophysical Journal* **597**, 1092–1096 (2003).
- [3] Pineda, J. S. & Villadsen, J. Coherent radio bursts from known M-dwarf planet-host YZ Ceti. *Nature Astronomy* **7**, 569–578 (2023).
- [4] Cohen, O. *et al.* The Dynamics of Stellar Coronae Harboring Hot Jupiters. I. A Time-dependent Magnetohydrodynamic Simulation of the Interplanetary Environment in the HD 189733 Planetary System. *The Astrophysical Journal* **733**, 67 (2011).
- [5] Rizzuto, A. C. *et al.* TESS Hunt for Young and Maturing Exoplanets (THYME). II. A 17 Myr Old Transiting Hot Jupiter in the Sco-Cen Association. *The Astronomical Journal* **160**, 33 (2020).
- [6] Barber, M. G. *et al.* TESS Investigation—Demographics of Young Exoplanets (TI-DYE). II. A Second Giant Planet in the 17 Myr System HIP 67522. *The Astrophysical Journal* **973**, L30 (2024).
- [7] Thao, P. C. *et al.* The Featherweight Giant: Unraveling the Atmosphere of a 17 Myr Planet with JWST. *The Astronomical Journal* **168**, 297 (2024).
- [8] de Zeeuw, P. T., Hoogerwerf, R., de Bruijne, J. H. J., Brown, A. G. A. & Blaauw, A. A HIPPARCOS Census of the Nearby OB Associations. *The Astronomical Journal* **117**, 354–399 (1999).

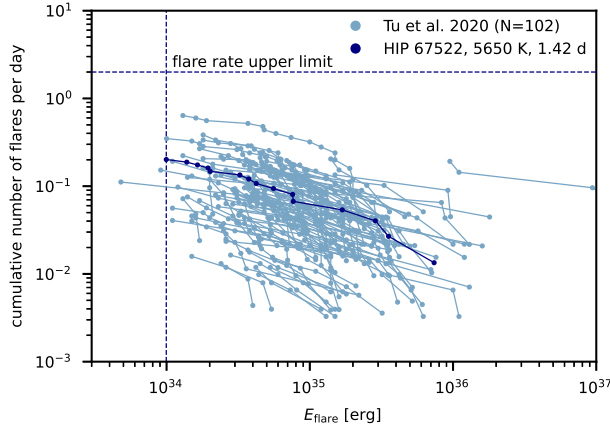


Extended Data Figure 5: Planet-induced emission power. Estimate of planet-induced power (overlapping blue solid lines) as a function of highest possible induced flare energy E_{\max} . Lower lines indicate a smaller lower limit for the energy of planet-induced flares in the range $10^{32} - 10^{33}$ erg. Below this limit, flares cannot be distinguished from X-ray quiescent emission [28]. The flares on HIP 67522 are distributed following a power law distribution with slope < 2 , so that the total power integrated over the distribution is determined by the high energy tail of the distribution, i.e., by E_{\max} . The measured power is incompatible with the power expected from the Alfvén wing star-planet interaction mechanism [1] (blue shade), and must therefore tap into a different energy source, e.g., the energy stored in pre-flare coronal loops. The X-ray quiescent emission indicates an estimate of the energy budget available to the interaction (dotted line).

- [9] Gaia Collaboration *et al.* Gaia Early Data Release 3. Summary of the contents and survey properties. *Astronomy and Astrophysics* **649**, A1 (2021).
- [10] Ilin, E., Poppenhäger, K., Chebly, J., Ilić, N. & Alvarado-Gómez, J. D. Planetary perturbers: Flaring star-planet interactions in Kepler and TESS. *Monthly Notices of the Royal Astronomical Society* **527**, 3395–3417 (2024).
- [11] Strugarek, A. *et al.* MOVES V. Modelling star-planet magnetic interactions of HD 189733. *Monthly Notices of the Royal Astronomical Society* **512**, 4556–4572 (2022).
- [12] Zarka, P. Plasma interactions of exoplanets with their parent star and associated radio emissions. *Planetary and Space Science* **55**, 598–617 (2007).
- [13] Vedantham, H. K. *et al.* Coherent radio emission from a quiescent red dwarf indicative of star–planet interaction. *Nature Astronomy* **4**, 577–583 (2020).



Extended Data Figure 6: CME-induced mass loss rate. Estimate of mass loss rate from HIP 67522 b due to CMEs as a function of opening angle and efficiency η , assuming all CMEs intercept the planet's location. The shaded region marks the range of typical opening angles of solar CMEs [34]. The orange line highlights the assumed efficiency factor of $\eta = 0.1$, and the black dashed line indicates a 100% increase in mass loss rate compared to XUV-driven mass loss only.



Extended Data Figure 7: Flare rates of stars similar to HIP 67522. Flare frequency distributions of G dwarf stars with rotation periods $0.27 - 5.41$ d, and effective temperatures $5113 - 5916$ K with at least three flares observed with TESS [44], excluding known eclipsing binaries from [51]. We set the upper limit on the flare rates λ_0 and λ_1 conservatively to 2 d^{-1} (horizontal dashed line) above the minimum flare energy in the sample (vertical dashed line). Note that the [44] sample still likely contains binary stars, such that the true flare rate of some stars is lower than shown.

- [14] Fischer, C. & Saur, J. Time-variable Electromagnetic Star-Planet Interaction: The TRAPPIST-1 System as an Exemplary Case. *The Astrophysical Journal* **872**, 113 (2019).
- [15] Shkolnik, E., Bohlender, D. A., Walker, G. A. H. & Collier Cameron, A. The On/Off Nature of Star-Planet Interactions. *The Astrophysical Journal* **676**, 628–638 (2008).
- [16] Ricker, G. R. *et al.* Transiting Exoplanet Survey Satellite (TESS). *Journal of Astronomical Telescopes, Instruments, and Systems* **1**, 014003 (2015).
- [17] Benz, W. *et al.* The CHEOPS mission. *Experimental Astronomy* **51**, 109–151 (2021).
- [18] Gehrels, N. Confidence Limits for Small Numbers of Events in Astrophysical Data. *The Astrophysical Journal* **303**, 336 (1986).
- [19] Heitzmann, A. *et al.* The obliquity of HIP 67522 b: A 17 Myr old transiting hot Jupiter-sized planet. *The Astrophysical Journal Letters* **922**, L1 (2021).
- [20] Lanza, A. F. Star-planet magnetic interaction and activity in late-type stars with close-in planets. *Astronomy and Astrophysics* **544**, A23 (2012).
- [21] Boro Saikia, S. *et al.* Direct evidence of a full dipole flip during the magnetic cycle of a sun-like star. *Astronomy and Astrophysics* **620**, L11 (2018).
- [22] Bellotti, S. *et al.* Monitoring the large-scale magnetic field of AD Leo with SPIRou, ESPaDOnS, and Narval. Towards a magnetic polarity reversal? *Astronomy and Astrophysics* **676**, A56 (2023).
- [23] Osten, R. A. & Wolk, S. J. Connecting Flares and Transient Mass-loss Events in Magnetically Active Stars. *The Astrophysical Journal* **809**, 79 (2015).
- [24] Tristan, I. I. *et al.* A 7 Day Multiwavelength Flare Campaign on AU Mic. I. High-time-resolution Light Curves and the Thermal Empirical Neupert Effect. *The Astrophysical Journal* **951**, 33 (2023).
- [25] Kowalski, A. F. *et al.* Rising Near-ultraviolet Spectra in Stellar Megaflares. *The Astrophysical Journal* **978**, 81 (2025).
- [26] Vidotto, A. A. The evolution of the solar wind. *Living Reviews in Solar Physics* **18**, 3 (2021).
- [27] Lanza, A. F. Stellar coronal magnetic fields and star-planet interaction. *Astronomy and Astrophysics* **505**, 339–350 (2009).
- [28] Maggio, A. *et al.* XUV irradiation of young planetary atmospheres. Results from a joint XMM-Newton and HST observation of HIP67522. *Astronomy and*

Astrophysics **690**, A383 (2024).

- [29] Moschou, S.-P. *et al.* The Stellar CME-Flare Relation: What Do Historic Observations Reveal? *The Astrophysical Journal* **877**, 105 (2019).
- [30] Hazra, G., Vidotto, A. A., Carolan, S., Villarreal D’Angelo, C. & Manchester, W. The impact of coronal mass ejections and flares on the atmosphere of the hot Jupiter HD189733b. *Monthly Notices of the Royal Astronomical Society* **509**, 5858–5871 (2022).
- [31] Cohen, O. *et al.* Space-weather-driven Variations in Ly α Absorption Signatures of Exoplanet Atmospheric Escape: MHD Simulations and the Case of AU Mic b. *The Astrophysical Journal* **934**, 189 (2022).
- [32] Bisikalo, D. V. & Cherenkov, A. A. The influence of coronal mass ejections on the gas dynamics of the atmosphere of a "hot Jupiter" exoplanet. *Astronomy Reports* **60**, 183–192 (2016).
- [33] Cherenkov, A., Bisikalo, D., Fossati, L. & Möstl, C. The Influence of Coronal Mass Ejections on the Mass-loss Rates of Hot-Jupiters. *The Astrophysical Journal* **846**, 31 (2017).
- [34] Jang, S., Moon, Y. J., Kim, R. S., Lee, H. & Cho, K. S. Comparison between 2D and 3D Parameters of 306 Front-side Halo CMEs from 2009 to 2013. *The Astrophysical Journal* **821**, 95 (2016).
- [35] Brandeker, A., Patel, J. A. & Morris, B. M. PIPE: Extracting PSF photometry from CHEOPS data. *Astrophysics Source Code Library* ascl:2404.002 (2024).
- [36] Kreidberg, L. Batman: BAsic Transit Model cAlculatioN in Python. *Publications of the Astronomical Society of the Pacific* **127**, 1161 (2015).
- [37] McKinney, W. Data Structures for Statistical Computing in Python. *Proceedings of the 9th Python in Science Conference* 56–61 (2010).
- [38] Savitzky, Abraham. & Golay, M. J. E. Smoothing and Differentiation of Data by Simplified Least Squares Procedures. *Analytical Chemistry* **36**, 1627–1639 (1964).
- [39] Mendoza, G. T., Davenport, J. R. A., Agol, E., Jackman, J. A. G. & Hawley, S. L. Llamaradas Estelares: Modeling the Morphology of White-light Flares. *The Astronomical Journal, Volume 164, Issue 1, id.17, 12 pp.* **164**, 17 (2022).
- [40] Foreman-Mackey, D., Hogg, D. W., Lang, D. & Goodman, J. Emcee: The MCMC Hammer. *Publications of the Astronomical Society of the Pacific* **125**, 306 (2013).
- [41] Shibayama, T. *et al.* Superflares on Solar-type Stars Observed with Kepler. I. Statistical Properties of Superflares. *The Astrophysical Journal Supplement Series* **209**, 5 (2013).

- [42] Howard, W. S. *et al.* EvryFlare. III. Temperature Evolution and Habitability Impacts of Dozens of Superflares Observed Simultaneously by Evryscope and TESS. *The Astrophysical Journal* **902**, 115 (2020).
- [43] Rabello Soares, M. C., de Freitas, M. C. & Ferreira, B. P. L. Blackbody Temperature of 200+ Stellar Flares Observed with the CoRoT Satellite. *The Astronomical Journal* **164**, 223 (2022).
- [44] Tu, Z.-L., Yang, M., Zhang, Z. J. & Wang, F. Y. Superflares on Solar-type Stars from the First Year Observation of TESS. *The Astrophysical Journal* **890**, 46 (2020).
- [45] Ilin, E. *et al.* Flares in open clusters with K2. II. Pleiades, Praesepe, Ruprecht 147, and M 67. *Astronomy and Astrophysics* **645**, A42 (2021).
- [46] Reiners, A. *et al.* Magnetism, rotation, and nonthermal emission in cool stars. Average magnetic field measurements in 292 M dwarfs. *Astronomy and Astrophysics* **662**, A41 (2022).
- [47] DeRosa, M. L., Brun, A. S. & Hoeksema, J. T. Solar Magnetic Field Reversals and the Role of Dynamo Families. *The Astrophysical Journal* **757**, 96 (2012).
- [48] Lehmann, L. T., Hussain, G. A. J., Jardine, M. M., Mackay, D. H. & Vidotto, A. A. Observing the simulations: Applying ZDI to 3D non-potential magnetic field simulations. *Monthly Notices of the Royal Astronomical Society* **483**, 5246–5266 (2019).
- [49] Hackman, T., Lehtinen, J., Rosén, L., Kochukhov, O. & Käpylä, M. J. Zeeman-Doppler imaging of active young solar-type stars. *Astronomy and Astrophysics* **587**, A28 (2016).
- [50] Willamo, T. *et al.* Zeeman-Doppler imaging of five young solar-type stars. *Astronomy and Astrophysics* **659**, A71 (2022).
- [51] Ziegler, C. *et al.* SOAR TESS Survey. II. The Impact of Stellar Companions on Planetary Populations. *The Astronomical Journal* **162**, 192 (2021).

Extended Data Table 2: Orbital phase coverage of HIP 67522 b.

Orb. phase	Exposure time [d]	Orb. phase	Exposure time [d]
(0.0, 0.01]	0.997338	(0.5, 0.51]	0.493056
(0.01, 0.02]	1.239352	(0.51, 0.52]	0.486111
(0.02, 0.03]	1.260880	(0.52, 0.53]	0.529514
(0.03, 0.04]	1.251157	(0.53, 0.54]	0.657870
(0.04, 0.05]	1.251273	(0.54, 0.55]	0.670602
(0.05, 0.06]	1.274074	(0.55, 0.56]	0.685532
(0.06, 0.07]	1.204398	(0.56, 0.57]	0.729514
(0.07, 0.08]	1.158333	(0.57, 0.58]	0.732870
(0.08, 0.09]	0.924421	(0.58, 0.59]	0.732755
(0.09, 0.1]	0.664468	(0.59, 0.6]	0.733681
(0.1, 0.11]	0.626389	(0.6, 0.61]	0.739699
(0.11, 0.12]	0.626389	(0.61, 0.62]	0.738657
(0.12, 0.13]	0.625000	(0.62, 0.63]	0.759722
(0.13, 0.14]	0.627778	(0.63, 0.64]	0.759722
(0.14, 0.15]	0.626389	(0.64, 0.65]	0.765278
(0.15, 0.16]	0.627778	(0.65, 0.66]	0.763889
(0.16, 0.17]	0.626389	(0.66, 0.67]	0.708333
(0.17, 0.18]	0.626389	(0.67, 0.68]	0.694444
(0.18, 0.19]	0.625000	(0.68, 0.69]	0.695833
(0.19, 0.2]	0.626389	(0.69, 0.7]	0.665278
(0.2, 0.21]	0.625000	(0.7, 0.71]	0.658333
(0.21, 0.22]	0.625000	(0.71, 0.72]	0.722222
(0.22, 0.23]	0.626389	(0.72, 0.73]	0.738657
(0.23, 0.24]	0.626389	(0.73, 0.74]	0.734028
(0.24, 0.25]	0.626389	(0.74, 0.75]	0.721412
(0.25, 0.26]	0.626389	(0.75, 0.76]	0.721644
(0.26, 0.27]	0.655324	(0.76, 0.77]	0.732986
(0.27, 0.28]	0.677315	(0.77, 0.78]	0.736806
(0.28, 0.29]	0.695602	(0.78, 0.79]	0.781829
(0.29, 0.3]	0.697338	(0.79, 0.8]	0.788773
(0.3, 0.31]	0.699306	(0.8, 0.81]	0.853704
(0.31, 0.32]	0.710648	(0.81, 0.82]	0.796065
(0.32, 0.33]	0.725231	(0.82, 0.83]	0.742708
(0.33, 0.34]	0.739005	(0.83, 0.84]	0.736921
(0.34, 0.35]	0.743171	(0.84, 0.85]	0.737269
(0.35, 0.36]	0.714699	(0.85, 0.86]	0.712847
(0.36, 0.37]	0.698148	(0.86, 0.87]	0.658333
(0.37, 0.38]	0.689120	(0.87, 0.88]	0.618519
(0.38, 0.39]	0.660648	(0.88, 0.89]	0.622222
(0.39, 0.4]	0.659838	(0.89, 0.9]	0.626389
(0.4, 0.41]	0.663194	(0.9, 0.91]	0.620833
(0.41, 0.42]	0.646644	(0.91, 0.92]	0.655556
(0.42, 0.43]	0.625000	(0.92, 0.93]	0.687500
(0.43, 0.44]	0.625000	(0.93, 0.94]	0.686111
(0.44, 0.45]	0.626389	(0.94, 0.95]	0.739120
(0.45, 0.46]	0.616667	(0.95, 0.96]	0.879514
(0.46, 0.47]	0.625000	(0.96, 0.97]	0.872222
(0.47, 0.48]	0.625000	(0.97, 0.98]	0.864352
(0.48, 0.49]	0.622222	(0.98, 0.99]	0.852315
(0.49, 0.5]	0.620833	(0.99, 1.0]	0.858796

The unbinned phase coverage table is provided online.

Extended Data Table 3: TESS and CHEOPS flares.

Mission	t_{peak} [BJD] [*]	a^{\dagger}	$\log_{10} E$ [erg] [‡]	orb. phase
CHEOPS	2460392.789	0.048	$35.9^{+0.03}_{-0.04}$	0.025884
CHEOPS	2460400.003	0.012	$34.9^{+0.04}_{-0.04}$	0.062428
CHEOPS	2460455.637	0.003	$34.1^{+0.09}_{-0.12}$	0.056482
CHEOPS	2460413.181	0.002	$33.3^{+0.07}_{-0.08}$	0.955996 excluded [§]
TESS	2458608.290	0.005	$34.6^{+0.04}_{-0.04}$	0.612894
TESS	2458609.676	0.011	$34.7^{+0.07}_{-0.04}$	0.812154
TESS	2459334.890	0.010	$35.2^{+0.07}_{-0.08}$	0.017420
TESS	2459334.981	0.024	$35.5^{+0.05}_{-0.05}$	0.030477
TESS	2459335.173	0.006	$34.9^{+0.10}_{-0.14}$	0.058039
TESS	2459342.014	0.008	$34.6^{+0.04}_{-0.05}$	0.041006
TESS	2460042.757	0.005	$34.3^{+0.06}_{-0.07}$	0.730162
TESS	2460044.282	0.005	$34.5^{+0.05}_{-0.05}$	0.949207
TESS	2460045.424	0.003	$34.0^{+0.09}_{-0.11}$	0.113382
TESS	2460052.991	0.004	$34.3^{+0.05}_{-0.06}$	0.200551
TESS	2460059.608	0.049	$35.5^{+0.04}_{-0.04}$	0.151479
TESS	2460065.829	0.004	$34.2^{+0.06}_{-0.07}$	0.045315

^{*}Time of best-fit flare peak time.

[†]Best-fit relative flare amplitude.

[‡]Best-fit bolometric flare energy with 16th and 84th percentile uncertainties.

[§]Flare was excluded from the statistical analysis because it was below the detection threshold of TESS.